ADVANCED
SCIENCE NEWS
www.advancedsciencenews.com

NANO | MICRO
small

Energy Storage

Mesoporous NiS$_2$ Nanospheres Anode with Pseudocapacitance for High-Rate and Long-Life Sodium-Ion Battery

Ruimin Sun, Sijie Liu, Qiulong Wei, Jinzhi Sheng, Shaohua Zhu, Qinyou An,* and Liqiang Mai*

It is of great importance to exploit electrode materials for sodium-ion batteries (SIBs) with low cost, long life, and high-rate capability. However, achieving quick charge and high power density is still a major challenge for most SIBs electrodes because of the sluggish sodiation kinetics. Herein, uniform and mesoporous NiS$_2$ nanospheres are synthesized via a facile one-step polyvinylpyrrolidone assisted method. By controlling the voltage window, the mesoporous NiS$_2$ nanospheres present excellent electrochemical performance in SIBs. It delivers a high reversible specific capacity of 692 mA h g^{-1}. The NiS$_2$ anode also exhibits excellent high-rate capability (253 mA h g^{-1} at 5 A g^{-1}) and long-term cycling performance (319 mA h g^{-1} capacity remained even after 1000 cycles at 0.5 A g^{-1}). A dominant pseudocapacitance contribution is identified and verified by kinetics analysis. In addition, the amorphization and conversion reactions during the electrochemical process of the mesoporous NiS$_2$ nanospheres is also investigated by in situ X-ray diffraction. The impressive electrochemical performance reveals that the NiS$_2$ offers great potential toward the development of next generation large scale energy storage.

1. Introduction

Nowadays, electric energy storage devices and smart grids are quite common applications in modern society that utilize renewable energy storage with rechargeable batteries, an the demand is large and the market is broad.[1–4] Among the diverse energy storage devices, lithium-ion batteries (LIBs)

are particularly attractive due to their high energy and power densities that are used to massive energy storage systems.[5–7] However, the disadvantage of LIBs is lack of lithium source and it restricts the application for energy storage.[8] Under this circumstance, room-temperature sodium-ion batteries (SIBs) are emerging as appealing energy storage systems owing to the low cost, widespread reserves of sodium resources.[9–13] Compared with LIBs, the specific capacity, rate capability, and cycle life of SIBs are less desirable owing to the larger radius of the sodium ion, which restricts the electrochemical reaction kinetics and extensively decreases the convenience to find appropriate host materials for reversible and rapid Na$^+$ energy storage.[14–16] Herein, it is an urgent need but still a major challenge to rationally explore and delicately design appropriate materials with both high capacity and long cycle life for advanced SIBs, especially for anode materials. In recent years, the anode materials of SIBs have been intensively investigated. Up to now, a number of studies show that the intercalation-type anode materials (graphite,[17] Na$_3$V$_2$(PO$_4$)$_3$,[18] Na$_2$Ti$_3$O$_7$[19]) exhibit well cycling and rate performance but low theoretical capacity. Conversion-type

R. M. Sun, S. J. Liu, Dr. Q. L. Wei, J. Z. Sheng,
S. H. Zhu, Prof. Q. Y. An, Prof. L. Q. Mai
State Key Laboratory of Advanced Technology
for Materials Synthesis and Processing
Wuhan University of Technology
Hubei, Wuhan 430070, P. R. China
E-mail: anqinyou86@whut.edu.cn; mlq518@whut.edu.cn
Dr. L. Q. Mai
Department of Chemistry
University of California
Berkeley, CA 94720, USA

The ORCID identification number(s) for the author(s) of this article can be found under https://doi.org/10.1002/smll.201701744.

(ZnO,[20] MoS$_3$,[21] etc.) and alloy-type anode materials (P,[22] SnO$_2$,[23] etc.) present high theoretical capacity. However, severe capacity fading limits their application owing to the large volume changes or the sluggish kinetics during sodiation/desodiation process.[21,24–27]

Transition metal dichalcogenides (TMDs) have received much attention because of their remarkable characteristics, such as unique electronic structure, high electrical conductivity, and rich redox chemistry. These properties make them become promising for Na$^+$ storage. Recently, some typical TMDs electrode materials for batteries have been reported, such as FeS$_2$,[28] MoS$_2$,[25] TiS$_2$,[29] etc. As an important member of TMDs, nickel disulfides (NiS$_2$) has great superiority for practical energy storage due to its high theoretical capacity, low cost, and environmental friendliness. However, as a conversion-type anode material, NiS$_2$ anode shows inferior electrochemical performance. To solve these problems, many efforts have been made, such as compositing metal disulfides with a carbon matrix. Wang and co-workers[30] reported nickel disulfides-graphene nanosheets composites for SIBs, which deliver enhanced performance than single NiS$_2$, a steady capacity ≈400 mAh g^{-1} at 100 mA g^{-1}, and rate performance of 168 mAh g^{-1} at 1.6 A g^{-1} are obtained. Nevertheless, the electrochemical performances are not very satisfactory, a smart strategy to develop nickel disulfides anode with high performance is urgently desired. Furthermore, some detailed sodium storage mechanisms still need to be further explored. Currently, 3D NiS$_2$ nanospheres with numerous pores were designed as anode materials. The nanosized NiS$_2$ can offer large contact areas between electrode and electrolyte, shorten Na$^+$ and electron diffusion paths, leading to high rate performance. On the other hand, the proper pores are benefit to alleviate the large volume changes during electrochemical process, which are favorable to gain longer cycling stability. By combining nanosized active materials with 3D network, some encouraging advances have been achieved in SIBs. Reducing the electrochemical window is also a strategy to improve the performance of TMDs and other electrode materials.[31,32] Deep sodium sodiation/desodiation results in more serious voltage drop and electrochemical polarization. By optimizing the voltage window, the moderate volume change and better cycling performance are obtained. Besides, the battery can present partial capacitive behavior which improves the rate and cyclic properties.[32,33] Therefore, it is crucial to identify new electrode materials and appropriate voltage window to further optimize the electrochemical performance of the electrode material.

Herein, uniform and mesoporous NiS$_2$ nanospheres are synthesized via a facile one-step polyvinylpyrrolidone (PVP) assisted method. With porous nanostructure for fast sodium ion diffusion and buffering the volume change during the electrochemical process, the NiS$_2$ mesoporous nanospheres present excellent electrochemical performance in SIBs. It delivers a high specific capacity of 702 mA h g^{-1} at 0.1A g^{-1}. The anode also exhibits excellent high-rate capability (253 mA h g^{-1} at 5 A g^{-1}) and superior long-life performance (689 mA h g^{-1} after 1000 cycles at 0.5 A g^{-1}). The structure changes of electrode also have been investigated by in situ X-ray diffraction (XRD) during the electrochemical process. Furthermore, a detailed electrochemical kinetic analysis is performed to explore the nature of the charge storage process.

2. Results and Discussion

Figure 1 schematically illustrates the formation of uniform and mesoporous NiS$_2$ nanospheres. It is worth mentioning that the effect of PVP is important for the formation process of spherical shape and monodispersity of NiS$_2$ nanospheres. Without PVP, NiS$_2$ grows into heterogeneous balls which are adhesive together (Figure S1, Supporting Information). PVP is a great surfactant during the synthesis of NiS$_2$ nanospheres owing to its hydroxyl at the ends of the molecules. The formation mechanism of NiS$_2$ was examined by the help of time-dependent experiments. Scanning electron microscope (SEM) images obtained at different reaction time are shown in Figure S2, Supporting Information. In brief, NiS$_2$ is solvothermally prepared by reacting Ni^{2+} and S$_2$O$_3^{2-}$, in which S$_2$O$_3^{2-}$ is chosen to serve as both reducing agent and sulfur source. Ethylene glycol as solvent can be converted into acetaldehyde at high temperature, which serves as oxidizing agent. The XRD patterns of the samples obtained in different solvents have been presented (Figure S3, Supporting Information). The samples obtained at ethylene glycol (EG) and H$_2$O-EG mixed solvents show pure NiS$_2$ phase, while the sample obtained at distilled water is the impure phase. EG solvent is critical for the formation of NiS$_2$. The specific chemical reaction is discussed in Section S1, Supporting Information. The surfactant PVP with the hydrophobic vinyl group and hydrophilic carbonyl group results in the formation of polarized nuclei. The numerous precursor nuclei are absorbed on the carbonyl groups of PVP, then gradually become more tightly packed. With further processing,
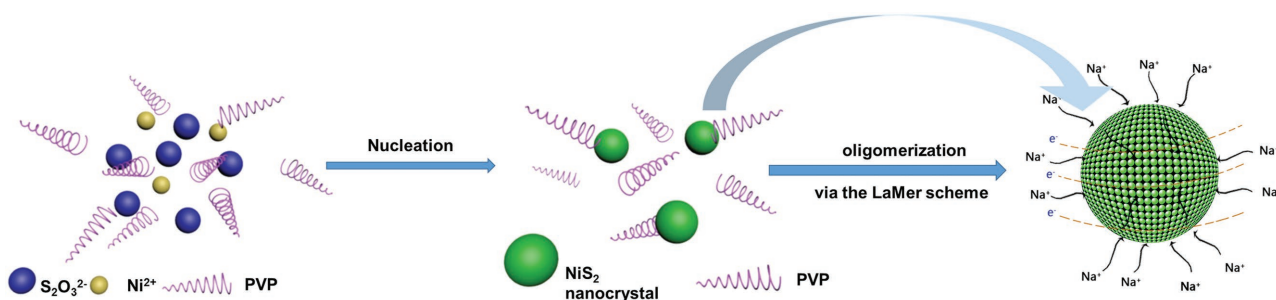

Figure 1. Schematic illustration for the growth of mesoporous NiS$_2$ nanosphere.

hierarchical spherical shape and monodispersed NiS_2 nanospheres form with tiny nanocrystals oligomerization via the LaMer scheme.[34–36] In this reaction, PVP is critical in tuning the morphology and preventing the particles aggregation. Its steric hindrance effect origined from its hydrophobic carbon chains hinders the aggregation of particles.[37] The SEM images of the as-prepared NiS_2 nanospheres with different PVP amounts during synthesis are also displayed (Figure S4, Supporting Information). With the increase of the amount of PVP from 0.4 to 1 g, no obvious morphology difference can be observed. The results confirm that the amount of PVP is not a vital role on controlling the size and morphology of the NiS_2 nanospheres. Another interesting finding is that the viscosity of the solvent is of great importance for NiS_2 morphology formation. When using either distilled water or EG as solvent, the ideal morphology can hardly be synthesized (Figure S5, Supporting Information). Hence, by using mixed solution of water and EG as solvent, which has the regulated viscosity, the well monodispersed NiS_2 nanospheres can be fabricated.

The phase of the as-prepared sample was identified by XRD (**Figure 2**a). All the characteristic peaks of NiS_2 can be indexed into cubic NiS_2 phase (space group: Pa-3) with lattice constants $a = b = c = 5.68$ Å (JCPDF No. 01–089–1495) without impurity. According to Figure 2b, the nitrogen sorption isotherms were measured to verify the pore structure of the hierarchical spherical mesoporous NiS_2. The product shows a relatively high specific Brunauer–Emmett–Teller (BET) surface area of 49.1 m^2 g^{-1} and pore volume of 0.143 cm^3 g^{-1}. The nitrogen adsorption–desorption curve of NiS_2 exhibits a typical hysteresis loop that can be linked to the slit-shaped pores. The pore sizes are mainly distributed between 3 and 4 nm (the inset of Figure 2b). Figure 2c shows the SEM images and the size distribution of the as-prepared NiS_2 nanospheres. The NiS_2 nanospheres have major diameters of 90–140 nm. SEM images (Figure 2d) recorded at high magnification clearly show the ideal spherical shape of the NiS_2, with uniform shapes and uniform distribution. A single NiS_2 nanosphere is composed of tightly aggregated nanocrystals with the size of 10 nm and has highly ordered pore structures according to the inset of Figure 2d. The morphology and detailed crystal structure of NiS_2 are further revealed by transmission electron microscopy (TEM) (Figure 2e) and high-resolution transmission electron microscopy (HRTEM) (Figure 2f). Figure 2e shows that a batch of pores forms in the synthesized NiS_2. These pores are about 4 nm in size, which correspond to the BET results. Also, we can see the channels near the surface, which are formed by the piled NiS_2 nanocrystals (less than 10 nm size). As shown in the Figure 2f, the lattice fringes of NiS_2 display interplanar spacing of 3.28 Å in the particle, which match well with the (111) planes of the NiS_2. This mesoporous architecture has tremendous superiority in ion diffusion and electron transport during the electrochemical process, owing to its large contact area with the electrolyte and its cushion function to buffer the volume change during the cycling.[38]

The electrochemical performance of mesoporous NiS_2 nanospheres is shown in **Figure 3**. Cyclic voltammetry (CV) measurement for the first three cycles at 0.1 mV s^{-1} in the

diglyme (DGM) electrolyte was conducted to gain further insight into the electrochemistry of the NiS_2/Na cell (Figure 3a). A strong cathodic peak appears at 1.20 V and disappears in the following cycles, ascribing to the initial intercalation of Na^+ into the NiS_2 crystal. During the second and subsequent cycles, two pairs of broad peaks at 0.92/1.64 and 1.42/1.93 V can be observed, corresponding to the reduction of NiS_2.[39] The CV curves except the initial cycle are overlapped, demonstrating the high reversibility. Typical discharge and charge profiles of the NiS_2 electrode at 0.1 A g^{-1} are shown in Figure 3b, in which the potential plateaus match well with the CV curves in the corresponding electrochemical process. Figure 3c exhibits the cycling performance and corresponding Coulombic efficiency (CE) of NiS_2 at 0.1 A g^{-1}. As a result of the inevitable decomposition of the electrolyte and the formation of a solid electrolyte interface, the discharge capacity fades fast in the initial several cycles.[29,30,33] A reversible discharge capacity of 692 mAh g^{-1} (the 8th cycle) can be achieved at 0.1 A g^{-1}. The CE gradually increases to 100% after a few cycles and then can be stabilized. To investigate the rate performance of the NiS_2 nanosphere electrodes, electrochemical performance at progressively increased current density (ranging from 0.1 to 5 A g^{-1}) was measured (Figure 3d). Specific capacities of 681, 490, and 420 mAh g^{-1} at 0.3, 1, and 2 A g^{-1} can be obtained, respectively. Even at a high rate of 5 A g^{-1}, a specific capacity of 253 mAh g^{-1} can be achieved. When the current density turns back to 0.1 A g^{-1}, a large portion of the initial capacity can be recovered (534 mA h g^{-1} capacity can be recovered). The discharge and charge curves at different rates are shown in Figure S6, Supporting Information. Furthermore, the NiS_2 nanospheres also possess durable cycling stability. At a high current density of 0.5 A g^{-1}, a discharge capacity of 319 mAh g^{-1} can still be achieved after 1000 long cycles (Figure 3e). The discharge–charge curves of NiS_2 electrode after 1000 cycles are shown in Figure S7, Supporting Information. The electrochemical performance of mesoporous NiS_2 nanospheres stands out among those of previous reported nickel sulfide materials (**Table 1**). The Electrochemical impedance spectroscopy (EIS) spectra of the NiS_2 electrodes before and after cycling (Figure S8, Supporting Information) show a compressed semicircle in the high to medium frequency region of each spectrum, which corresponds to the charge transfer resistance (R_{ct}) of the electrode, and an ≈45° inclined line in the low frequency range which stands for the Warburg impendence (Z_w). The charge transfer resistance of NiS_2 becomes much lower after 100 cycles at 0.5 A g^{-1}. Additionally, the slope in the low frequency range is increased, indicating the enhanced ion diffusion kinetics. The SEM images of mesoporous NiS_2 nanospheres after 1st and 200 cycles are collected to study the structural stability (Figure S9, Supporting Information). No obvious morphology difference can be observed in SEM. The mesoporous nanosphere architecture is well maintained after long-term cycles, indicating the excellent structural stability of this NiS_2 electrode. The excellent electrochemical performance of NiS_2 is attributed to their unique structure. First, mesoporous NiS_2 nanospheres with larger surface area provide more active sites, larger electrode–electrolyte contact area, and enhance the charge transfer, resulting in rapid ion diffusion and high-rate
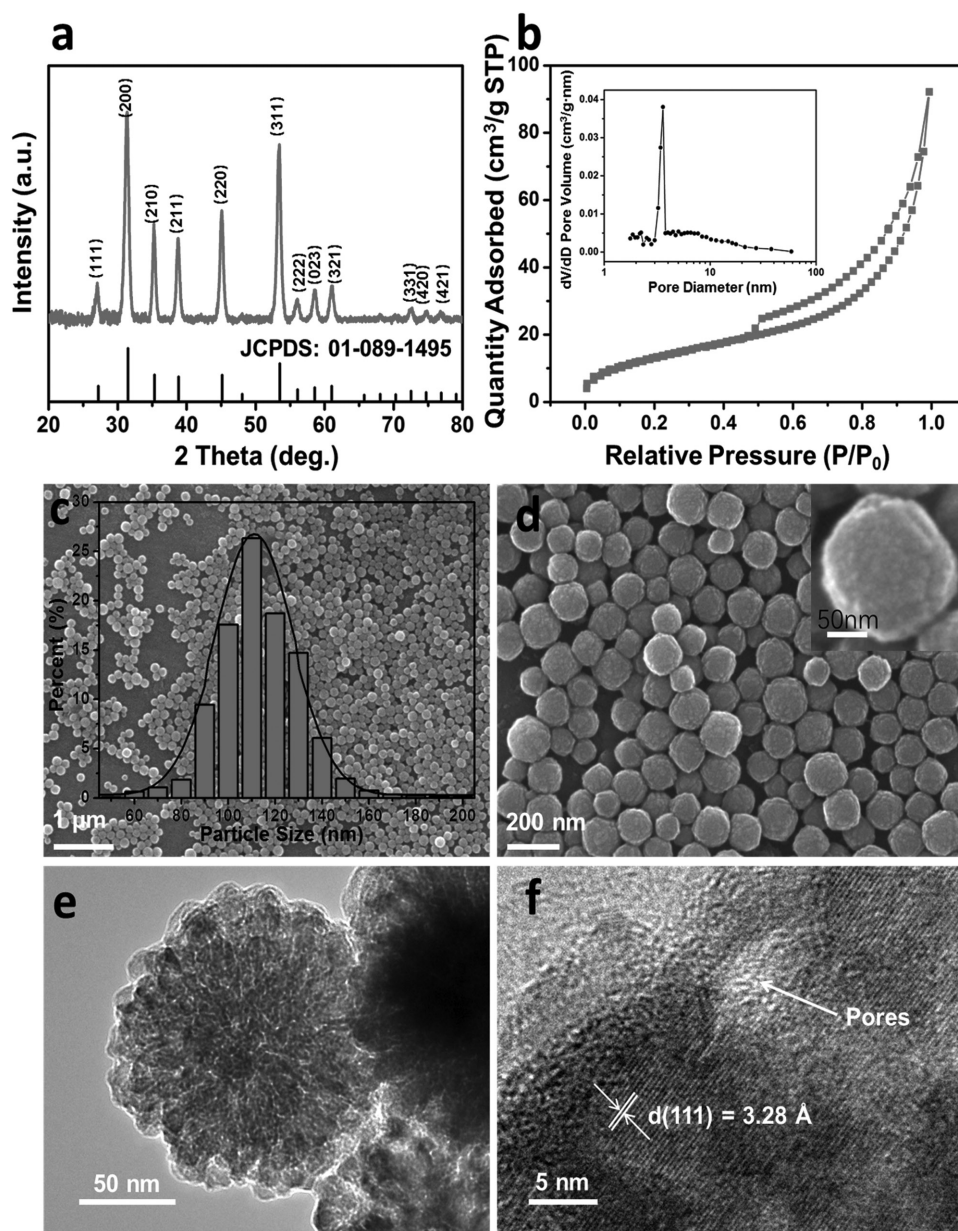
Figure 2. a) XRD patterns of NiS_2 nanospheres. b) Nitrogen adsorption–desorption isotherm of NiS_2 nanospheres (the inset is the pore size distribution of NiS_2 nanospheres). c) Size distributions and SEM image of NiS_2 nanospheres. d) High-magnification SEM images of NiS_2 nanospheres (the inset is a typical single NiS_2 nanosphere). e) TEM and f) HRTEM images of NiS_2 nanospheres.

capability. Second, the numerous pores in NiS_2 can offer free space for facile strain relaxation and volume expansion during cycling, which ensure the cycling stability. The selection of the electrolyte and the voltage window plays an important role to the improvement of the NiS_2 nanospheres charge storage. Figure S10 (Supporting Information) exhibits the discharge and charge curves of typical carbonate-based and ether-based electrolytes. The cells with carbonate-based electrolytes show high inferiority with large voltage polarization and rapid capacity decay. The EIS spectra (Figure S11, Supporting Information) of the NiS_2 electrodes in different electrolytes show that the NiS_2 electrode in the $NaSO_3CF_3$/DGM has the lowest R_{ct} among those typical carbonate-based and ether-based electrolytes. Figure S12 (Supporting Information) exhibits

the corresponding cycling performance. Through the contrast experiment, $NaClO_4$/DGM electrolyte can significantly improve the performance of NiS_2, showing comparable cyclability. This is in good accordance with previous results.[31,39] Compared to the voltage window of 0.4–2.9 V, the electrochemical performance of deeper discharge voltage to 0.01 V was also measured. High initial capacity is obtained, but the capacity fades fast with only 108 mAh g^{-1} capacity remained after 100 cycles at 0.1 A g^{-1} (Figure S13, Supporting Information). This means larger amount of Na ions participate in reaction, leading to larger volume change and more serious volume expansion. Ultimately, the combination of DGM electrolyte and terminal voltage of 0.4 V displays the best electrochemical performance in the measured system.
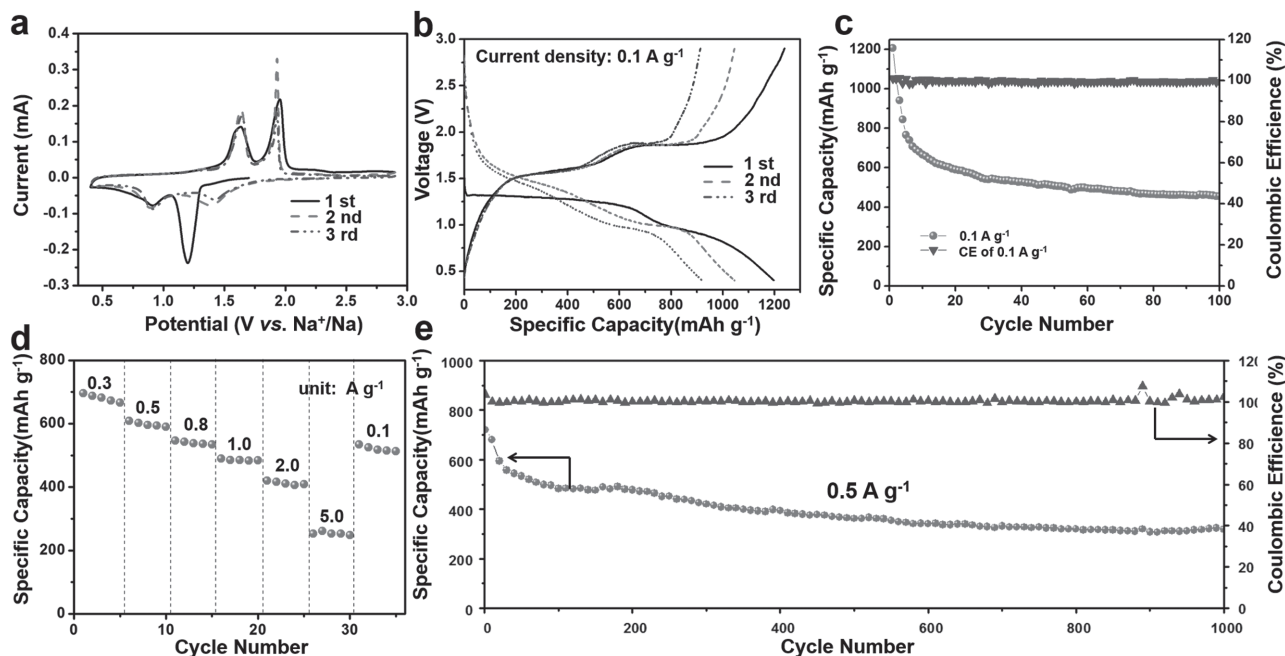
Figure 3. a) Cyclic voltammograms of NiS$_2$ material at the scan rate of 0.1 mV s^{-1}. b) Charge/discharge profiles of NiS$_2$ for the initial three cycle at 0.1 A g^{-1}. c) Discharge capacities and Coulombic efficiency versus cycle number of NiS$_2$ at 0.1 A g^{-1}. d) Rate performance of NiS$_2$. e) Discharge capacities and Coulombic efficiency versus cycle number of NiS$_2$ at 0.5A g^{-1}.

To further explore the nature of the charge storage process, CV measurements with different scan rate were conducted to investigate the electrochemical kinetics of the NiS$_2$ nanospheres.[39] The CV curves (**Figure 4**a) after the first cycle show similar broad peaks during both cathodic and anodic processes at each scan rate and display a slight peak shift while the scan rate increases from 0.2 to 1 mV s^{-1}, demonstrating low polarization of NiS$_2$ nanospheres in the DGM electrolyte. A related analysis can be performed regarding the behavior of the peak current by assuming that the current (*i*) obeys a power law relationship with the scan rate (*v*):[39]

$$i = av^b \tag{1}$$

In this equation, *a* is a constant, the *b*-value can change from 0.5 to 1. The *b*-value is given by the slope of the ln(*i*) versus ln(*v*) plots. If *b*-value approaches to 1, the system is mainly controlled by capacitance. If *b*-value is closed to 0.5, the diffusion process dominates. Figure 4b shows that the *b*-values at different oxidation and reduction states are 0.63 and 0.77, respectively. It indicates that the electrochemical reaction of NiS$_2$ nanospheres is controlled

by the combination of capacitive and diffusion processes. The *b*-value analysis for NiS$_2$ was performed using the CV data between 1.2 and 1.8 V (Figure S14, Supporting Information). The *b*-value is approached to 0.5 in the range of redox peaks, indicating that in the peak range the reaction is diffusion-controlled, while capacitive behavior dominates away from the peak range. A similar phenomenon was reported on ZnS nanospheres[39] and few-layer TiS$_2$ nanosheets.[29]

Another analysis is also performed to possibly determine the regions where the capacitive contributions occur according to the equation below:[42,43]

$$i(v) = k_1v + k_2v^{1/2} \tag{2}$$

Here, the total current response (*i*) at a fixed potential (*V*) can be separated into two mechanisms. The part of k_1v is the capacitive current. The diffusion-controlled current is reflected in $k_2v^{1/2}$. Figure 4c indicates that 85% of the total charge comes from capacitive contribution at a scan rate of 1 mV s^{-1} for NiS$_2$. The peak regions are predominately diffusion-controlled currents. The remaining regions

Table 1. Comparison of the electrochemical performance of the nickel sulfide SIB anodes reported in the literatures.

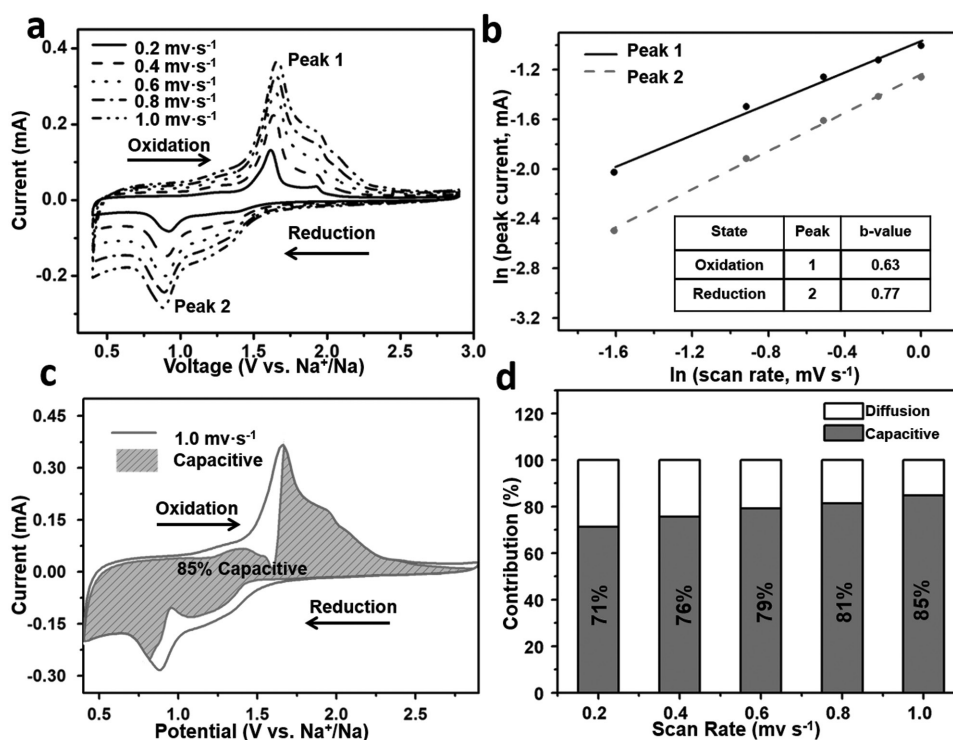| Reference	Sample	Voltage window	Capacity [mAh g^{-1}]	Rate capability
[40]	NiS$_x$-rGO composites	0.001–3 V	449 mAh g^{-1} at 300 mA g^{-1}	377 mAh g^{-1} at 3 A g^{-1}
[30]	NiS$_2$ graphene composites	0.001–3 V	407 mAh g^{-1} at 0.1 C	168 mAh g^{-1} at 2 C
[41]	NiS/rGO composites	0.005–3 V	701 mAh g^{-1} at 50 mA g^{-1}	181 mAh g^{-1} at 0.4 A g^{-1}
This work	Mesoporous NiS$_2$ nanospheres	0.4–2.9 V	692 mAh g^{-1} at 100 mA g^{-1}	253 mAh g^{-1} at 5 A g^{-1}

Figure 4. a) Cyclic voltammogram of the cell at different sweep rates. b) The fitted lines and ln(peak current) versus ln(scan rate) plot at different oxidation and reduction state. c) Cyclic voltammogram with the capacitive contribution to the total current shown by the shaded region. d) The capacity contribution at different scan rates (0.2, 0.4, 0.6, 0.8, and 1.0 mV s^{-1}). Results correspond to the cells with NiS$_2$ microspheres.

are almost entirely capacitive controlled, which is in accordance with the result of *b*-value. This obviously implies that mesoporous NiS$_2$ nanospheres offer many active surface sites, short sodium ion diffusion pathway as well as good electrolyte accessibility to all the electroactive surfaces due to the mesoporous structure and small nanoparticle size, resulting in the excellent electrochemical performance. The capacity contributions at different scan rates are shown in Figure 4d. The capacity contribution increases with the increasing of sweep rates. The kinetic analysis shows that a large portion of the stored charge comes from capacitive process.

The in situ X-ray diffraction technique was applied to further explore the electrochemical reaction mechanisms of NiS$_2$ electrode during cycling. For the in situ XRD (**Figure 5**), selected acquisition windows between 30° and 37° are chosen to in situ monitor the (200) and (210) diffractions of NiS$_2$ during the discharge/charge processes at 0.1 A g^{-1}. During the first discharge process, the (200) and (210) diffraction peaks slightly shift to lower angle. This typical single phase reaction represents the insertion of Na$^+$ into the NiS$_2$ (NiS$_2$ + xNa$^+$ + xe$^-$ → Na$_x$NiS$_2$). In the subsequent charge and discharge process, the main peaks of NiS$_2$ do not appear again, indicating that an irreversible conversion reaction occurs during the first cycle (Na$_x$NiS$_2$ + (4 − x) Na$^+$ + (4 − x) e$^-$ → Ni + 2Na$_2$S). No obvious Na$_2$S peaks were observed, indicating that an amorphous Na$_2$S phase was formed during sodiation. Meanwhile, nanocrystalline

Ni was also not detected owing to its very small crystallite size.[44–46] The initial two diffraction peaks disappear gradually until no obvious diffraction peak can be observed, demonstrating that the amorphization takes place during the latter cycling.

3. Conclusion

Uniform and mesoporous NiS$_2$ nanospheres are synthesized via a facile one-step PVP assisted method. The pores in NiS$_2$ nanospheres provide short ion diffusion paths, increase the contact area between electrode and electrolyte, and buffer volume change. Moreover, by reducing the voltage window and selecting a suitable ether-based electrolyte, the mesoporous NiS$_2$ nanospheres present excellent electrochemical performance as anode for SIBs. Kinetics analysis reveals a dominant pseudocapacitance contribution which is greatly beneficial to fast charge storage and long cycling stability. In addition, the amorphization and conversion reactions of the mesoporous NiS$_2$ nanospheres are further demonstrated by in situ X-ray diffraction. The remarkable electrochemical performance reveals that the NiS$_2$ is a promising anode for high-performance SIBs. These findings establish a good basis for the later research and open a new way for developing low cost battery systems for next-generation large scale energy storage.
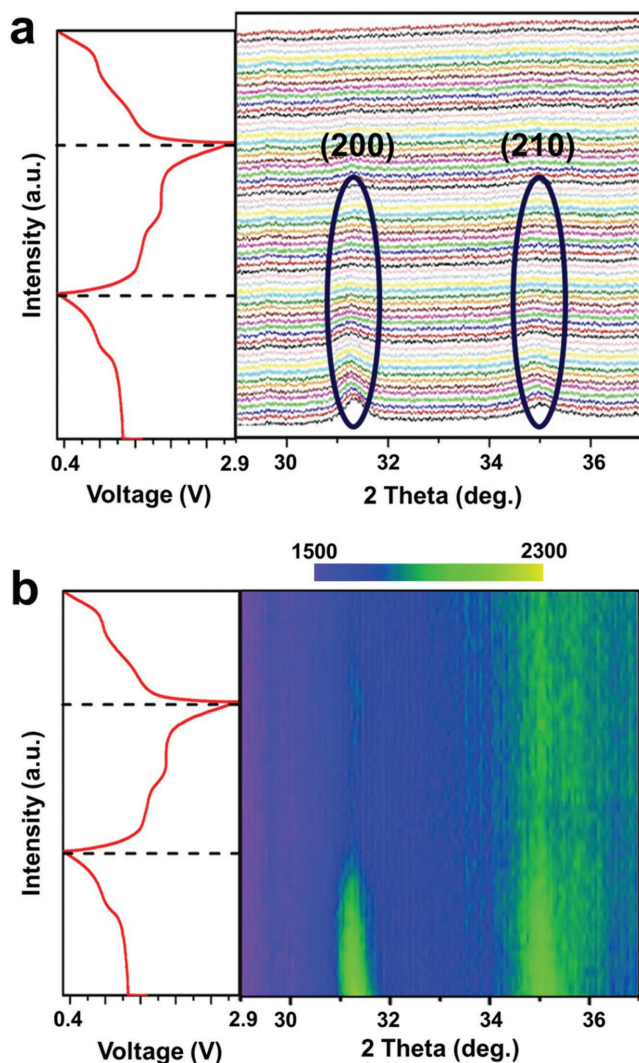
Figure 5. In situ XRD patterns of mesoporous NiS$_2$ nanospheres collected during galvanostatic discharge/charge half-cell. a,b) The image plot of diffraction patterns for (200) and (201) reflections at 100 mA g^{-1}. The corresponding voltage curve is plotted to the left.

4. Experimental Section

Synthesis of Mesoporous NiS$_2$ Nanospheres: In a typical synthesis, 0.6 g PVP K-30 was dissolved in the mixture of 40 mL EG and 40 mL distilled water. Then, 2 mmol C$_4$H$_6$O$_4$Ni·4H$_2$O and 6 mmol Na$_2$S$_2$O$_3$·5H$_2$O were added in the above mixed solution in sequence with continuous stirring. After that, the mixture was loaded into a Teflon-lined sealed autoclave and maintained at 180 °C for 12 h. The obtained suspension was centrifuged and the precipitate was washed thoroughly with water and absolute ethanol. The final product was dried at 80 °C for 10 h in a vacuum oven. For comparison, the product was synthesized using the same procedure without the addition of PVP K-30.

Material Characterizations: Powder XRD (D8 Advance X-ray diffractometer, Cu Kα X-ray source), field-emission scanning electron microscopy (SEM, JEOL-7100F) were used to characterize the structure and morphology of the as-prepared samples. TEM and HRTEM images were recorded using a JEM-2100F STEM/EDS microscope. BET surface area was measured by using Tristar ‖3020 instrument.

Electrochemical Measurements: Electrochemical measurements were performed with 2016 coin-type cells in an argon-filled glove box. The working electrode was obtained by mixing the as-prepared NiS$_2$, acetylene black, and carboxyl methyl cellulose in a weight ratio of 7:2:1. The slurry was then pasted onto a Ti foil. Glass fiber and sodium disks were employed as the separator and reference electrodes, respectively. Different kinds of electrolyte were used: (1) 1 M NaClO$_4$ in DGM; (2) 1 M NaClO$_4$ in ethylene carbonate and dimethyl carbonate with 5% fluoroethylene carbonate (EC:DMC = 1:1, v:v with 5.0% FEC); (3) 1 M NaPF$_6$ in propylene carbonate and ethylene carbonate (PC:EC = 1:1, v:v); and (4) 1 M NaClO$_4$ in PC and DMC (PC:DMC = 1:1, v:v). Galvanostatic measurements were performed over a potential range of 0.01/0.4−2.9 V versus Na$^+$/Na by using a multichannel battery testing system (LAND CT2001A). Cyclic voltammetry was tested by an electrochemical workstation (CHI 760D). Electrochemical impedance spectroscopy was conducted with Autolab potentiostat galvanostat (PGSTAT302N). All of the measurements were carried out at room temperature.

Supporting Information

Supporting Information is available from the Wiley Online Library or from the author.

Conflict of Interest

The authors declare no conflict of interest.

[1] D. Larcher, J. M. Tarascon, *Nat. Chem.* **2015**, *7*, 19.
[2] W. Xu, Z. Xie, X. Cui, K. Zhao, L. Zhang, L. Mai, Y. Wang, *Mater. Chem. A* **2016**, *4*, 3735.

[3] S. Xie, Z. Wang, F. Cheng, P. Zhang, W. Mai, Y. Tong, *Nano Energy* **2017**, *34*, 313.

[4] B. Dunn, H. Kamath, J. M. Tarascon, *Science* **2011**, *334*, 928.

[5] Z. Gao, N. Song, Y. Zhang, X. Li, *Nano Lett.* **2015**, *15*, 8194.

[6] Y. Lu, Z. Tu, L. A. Archer, *Nat. Mater.* **2014**, *13*, 961.

[7] K. Zhang, X. Han, Z. Hu, X. Zhang, Z. Tao, J. Chen, *Chem. Soc. Rev.* **2015**, *44*, 699.

[8] D. Chao, C. Zhu, P. Yang, X. Xia, J. Liu, J. Wang, X. Fan, S. V. Savilov, J. Lin, H. Fan, Z. Shen, *Nat. Commun.* **2016**, *7*, 12122.

[9] Z. Hu, L. Wang, K. Zhang, J. Wang, F. Cheng, Z. Tao, J. Chen, *Angew. Chem. Int. Ed.* **2014**, *53*, 12794.

[10] S. Fu, J. Ni, Y. Xu, Q. Zhang, L. Li, *Nano Lett.* **2016**, *16*, 4544.

[11] S. Li, Y. Dong, L. Xu, X. Xu, L. He, L. Mai, *Adv. Mater.* **2014**, *26*, 3358.

[12] J.-Y. Hwang, S.-M. Oh, S. T. Myung, K. Y. Chung, I. Belharouak, Y. K. Sun, *Nat. Commun.* **2015**, *6*, 6865.

[13] J. Qian, Y. Xiong, Y. Cao, X. Ai, H. Yang, *Nano Lett.* **2014**, *14*, 1865.

[14] M. S. Islam, C. A. J. Fisher, *Chem. Soc. Rev.* **2014**, *43*, 185.

[15] S. K. Das, S. Lau, L. A. Archer, *J. Mater. Chem. A* **2014**, *2*, 12623.

[16] M. Guignard, C. Didier, J. Darriet, P. Bordet, E. Elkaïm, C. Delmas, *Nat. Mater.* **2012**, *12*, 74.

[17] Y. Liu, N. Zhang, L. Jiao, Z. Tao, J. Chen, *Adv. Funct. Mater.* **2015**, *25*, 214.

[18] W. Duan, Z. Zhu, H. Li, Z. Hu, K. Zhang, F. Cheng, J. Chen, *J. Mater. Chem. A* **2014**, *2*, 8668.

[19] A. Rudola, K. Saravanan, C. W. Mason, P. Balaya, *J. Mater. Chem. A* **2013**, *1*, 2653.

[20] F. Zou, X. Hu, Z. Li, L. Qie, C. Hu, R. Zeng, Y. Jiang, Y. Huang, *Adv. Mater.* **2014**, *26*, 6622.

[21] L. Wang, K. Zhang, Z. Hu, W. Duan, F. Cheng, J. Chen, *Nano Res.* **2014**, *7*, 199.

[22] Y. Kim, Y. Park, A. Choi, N. S. Choi, J. Kim, J. Lee, J. Ryu, S. M. Oh, K. T. Lee, *Adv. Mater.* **2013**, *25*, 3045.

[23] M. Gu, A. Kushima, Y. Shao, J. G. Zhang, J. Liu, N. D. Browning, J. Li, C. Wang, *Nano Lett.* **2013**, *13*, 5203.

[24] M. T. McDowell, S. W. Lee, J. T. Harris, B. A. Korgel, C. Wang, W. D. Nix, Y. Cui, *Nano Lett.* **2013**, *13*, 758.

[25] R. Sun, Q. Wei, J. Sheng, C. Shi, Q. An, S. Liu, L. Mai, *Nano Energy* **2017**, *35*, 396.

[26] W. Kaveevivitchai, A. J. Jacobson, *Chem. Mater.* **2013**, *25*, 2708.

[27] H. J. Noh, Z. Chen, C. S. Yoon, J. Lu, K. Amine, Y. K. Sun, *Chem. Mater.* **2013**, *25*, 2109.

[28] A. Kitajoua, J. Yamaguchib, S. Harab, S. Okada, *J. Power Sources* **2014**, *247*, 391.

[29] J. E. Trevey, C. R. Stoldt, S. H. Lee, *J. Electrochem. Soc.* **2011**, *158*, A1282.

[30] T. Wang, P. Hu, C. Zhang, H. Du, Z. Zhang, X. Wang, S. Chen, J. Xiong, G. Cui, *ACS Appl. Mater. Interfaces* **2016**, *8*, 7811.

[31] Z. Hu, Z. Zhu, F. Cheng, K. Zhang, J. Wang, C. Chen, J. Chen, *Energy Environ. Sci.* **2015**, *8*, 1309.

[32] K. Zhang, Z. Hu, X. Liu, Z. Tao, J. Chen, *Adv. Mater.* **2015**, *27*, 3305.

[33] X. Wang, D. Chen, Z. Yang, X. Zhang, C. Wang, J. Chen, X. Zhang, M. Xue, *Adv. Mater.* **2016**, *28*, 8645.

[34] V. K. Lamer, R. H. Dinegar, *J. Am. Chem. Soc.* **1950**, *72*, 4847.

[35] Y. Cui, X. Lai, L. Li, Z. Hu, S. Wang, J. E. Halpert, R. Yu, D. Wang, *Chem. Phys. Chem.* **2012**, *13*, 2610.

[36] E. Uchaker, N. Zhou, Y. Li, G. Cao, *J. Phys. Chem. C* **2013**, *117*, 1621.

[37] K. M. K, S. Mourdikoudis, L. Polavarapu, S. E. Skrabalak, *Dalton Trans.* **2015**, *44*, 17883.

[38] X. W. D. Lou, L. A. Archer, Z. Yang, *Adv. Mater.* **2008**, *20*, 3987.

[39] D. Su, K. Kretschmer, G. Wang, *Adv. Energy Mater.* **2016**, *6*, 1501785.

[40] G. D. Park, J. S. Cho, Y. C. Kang, *Nanoscale* **2015**, *7*, 16781.

[41] Q. Pan, J. Xie, T. Zhu, G. Cao, X. Zhao, S. Zhang, *Inorg. Chem.* **2014**, *53*, 3511.

[42] J. B. Cook, H. S. Kim, Y. Yan, J. S. Ko, S. Robbennolt, B. Dunn, S. H. Tolbert, *Adv. Energy Mater.* **2016**, *6*, 1501937.

[43] H. S. Kim, J. B. Cook, H. Lin, J. S. Ko, S. H. Tolbert, V. Ozolins, B. Dunn, *Nat. Mater.* **2017**, *16*, 454.

[44] T. Zhou, W. K. Pang, C. Zhang, J. Yang, Z. Chen, H. K. Liu, Z. Guo, *ACS Nano* **2014**, *8*, 8323.

[45] R. Sun, Q. Wei, Q. Li, W. Luo, Q. An, J. Sheng, D. Wang, W. Chen, L. Mai, *ACS Appl. Mater. Interfaces* **2015**, *7*, 20902.

[46] C. Chen, X. Hu, Y. Jiang, Z. Yang, P. Hu, Y. Huang, *Chem. - Eur. J.* **2014**, *20*, 1383.